Article

Bulk Co_3O_4 for Methane Oxidation: Effect of the Synthesis Route on Physico-Chemical Properties and Catalytic Performance

Andoni Choya *[ID], Beatriz de Rivas, Jose Ignacio Gutiérrez-Ortiz [ID] and Rubén López-Fonseca

Chemical Technologies for Environmental Sustainability Group, Department of Chemical Engineering,
Faculty of Science and Technology, University of the Basque Country UPV/EHU, Barrio Sarriena s/n,
E-48940 Leioa, Bizkaia, Spain; beatriz.derivas@ehu.eus (B.d.R.); joseignacio.gutierrez@ehu.eus (J.I.G.-O.);
ruben.lopez@ehu.eus (R.L.-F.)
* Correspondence: andoni.choya@ehu.eus; Tel.: +34-94-601-3485

Abstract: The synthesis of bulk pure Co_3O_4 catalysts by different routes has been examined in order to obtain highly active catalysts for lean methane combustion. Thus, eight synthesis methodologies, which were selected based on their relatively low complexity and easiness for scale-up, were evaluated. The investigated procedures were direct calcination of two different cobalt precursors (cobalt nitrate and cobalt hydroxycarbonate), basic grinding route, two basic precipitation routes with ammonium carbonate and sodium carbonate, precipitation-oxidation, solution combustion synthesis and sol-gel complexation. A commercial Co_3O_4 was also used as a reference. Among the several examined methodologies, direct calcination of cobalt hydroxycarbonate (HC sample), basic grinding (GB sample) and basic precipitation employing sodium carbonate as the precipitating agent (CC sample) produced bulk catalysts with fairly good textural and structural properties, and remarkable redox properties, which were found to be crucial for their good performance in the oxidation of methane. All catalysts attained full conversion and 100% selectivity towards CO_2 formation at a temperature of 600 °C while operating at 60,000 h^{-1}. Among these, the CC catalyst was the only one that achieved a specific reaction rate higher than that of the reference commercial Co_3O_4 catalyst.

Keywords: methane; cobalt oxide; combustion; synthesis methodology; redox properties; lattice oxygen; thermal stability

1. Introduction

Natural gas for vehicles (NGV), also known as vehicular natural gas, is the name given to the natural gas applied as fuel for automotive. NGV presents numerous environmental and economic advantages in comparison with traditional liquid fuels (gasoline and diesel), even though it is also a fossil fuel. Firstly, it is relatively abundant. Some estimations value the world reserves of natural gas to be enough for more than 200 years at least, at current production and consumption rate [1]. Secondly, natural gas is considered the cleanest available fossil fuel. In this sense, vehicles fueled with NGV produce 20–30% and 50–80% less CO_2 and NO_x emissions, respectively, per kilometer than conventional fuels. In addition, it burns more cleanly, leading to virtually no emissions of particulate matter [2–4].

However, the consolidation of this type of vehicles in the automotive fleet requires the control of the residual (around 1%) unburned methane (main component of natural gas) emissions from the engine, since this gas possesses a powerful greenhouse effect potential. Because of the high chemical stability of this compound and its low concentration in the flue gases, low-temperature catalytic oxidation appears as an attractive solution for this purpose. The combustion of methane requires the activation of the C-H bonds in the methane molecule, which in turn require high reaction temperatures. However, the thermal level of the exhaust from a natural gas engine during normal operation does

not exceed 500–550 °C, well below the range for the purely thermal decomposition of this hydrocarbon [5,6]. Therefore, the selected catalysts are required to exhibit very high activity at relatively low temperatures and contact times, while also maintaining an excellent selectivity towards CO_2. Traditionally, the most commonly applied catalysts have been based on noble metals such as palladium. However, this type of catalysts is generally expensive and prone to deactivation, especially in the presence of water vapor [7,8].

For this reason, transition metal oxides are considered a promising alternative, owing to their lower cost, higher availability and relatively good activity for oxidation reactions. More specifically, spinel-type cobalt oxide (Co_3O_4) is a highly active catalyst for oxidation of CO and light hydrocarbons [9–11]. The main reason behind the increasing attention on this material is its strong Co^{3+}/Co^{2+} redox system that gives oxygen ions in its lattice a favored mobility. According to the available bibliography, methane oxidation over Co_3O_4 follows the Mars—van Krevelen mechanism. This means that methane is actually oxidized by the oxygen species present in the cobalt oxide lattice, generating oxygen vacancies. Then, the oxygen from the gas phase refills the oxygen vacancies provoking the subsequent reoxidation of the catalyst [12].

Spinel-type cobalt oxide can be synthesized by a wide number of both dry and wet synthetic routes, such as basic precipitation [13], sol-gel complexation [14], freeze-drying [15], solution combustion synthesis [16], reactive grinding [17], or simple calcination of a cobalt salt [18]. An appropriate synthesis route should ideally produce a cobalt oxide catalyst with suitable textural, structural and redox properties, which can be helpful in promoting its performance at low temperatures.

The objective of this work is to carry out a comprehensive study on bulk Co_3O_4 catalysts for the oxidation of lean methane that will include the preparation of a wide number of samples; their extensive characterization (N_2 physisorption, XRD, Raman spectroscopy, XPS, H_2-TPR and CH_4-TPRe) of the physical-chemical properties and the examination of its catalytic efficiency under demanding/realistic reaction conditions in terms of gas hourly space velocity (60,000 h^{-1}) and presence of water vapor in the inlet stream. For this purpose, eight Co_3O_4 samples were synthesized with various methodologies. The investigated routes were direct calcination of cobalt nitrate (DC) and cobalt hydroxycarbonate (HC), basic reactive grinding with ammonium hydrogen carbonate (GB), precipitation with ammonium carbonate (CN) and sodium carbonate (CC), wet precipitation-oxidation with sodium hydroxide (OW), solution combustion synthesis with glycine (SCS) and sol-gel complexation with citric acid (SG). Except for the HC sample, the used cobalt precursor was cobalt (II) nitrate hexahydrate. Additionally, a commercial Co_3O_4 sample was purchased from Alfa Aesar (COM), to serve as a reference. Note that the specific synthesis route followed for producing this sample was unknown. It is worth pointing out that these examined preparation methodologies were chosen among those with lower experimental complexity in order to facilitate a commercial application.

2. Results and Discussion

2.1. Physico-Chemical Characterisation of the Catalysts

The employed synthesis methodologies produced a family of eight bulk Co_3O_4 catalysts, which was complemented by a ninth commercial sample. The textural properties of these oxides in terms of specific surface area, pore volume and pore size distribution were determined by N_2 physisorption. The results are summarized in Table 1. All samples presented type IV isotherms (Figure S1, Supplementary Material) with H2 hysteresis cycles, although the hysteresis cycles were appreciably difficult to discern due to the low adsorbed volume of some of the oxides. The specific surface area varied from 5 to 16 m^2 g^{-1}. The pore volume followed a relatively consistent trend with respect to the surface area. Thus, the samples with the lowest specific surface area (DC and SG samples) also showed the smallest pore volume values (0.02 and 0.01 cm^3 g^{-1}, respectively), while the sample with the highest specific surface area (GB sample) also presented the largest pore volume (0.10 cm^3 g^{-1}). Nevertheless, some discrepancies to this trend were found that could be attributed to the

differences in the mean pore diameter. For instance, despite the fact that both CC and SCS samples exhibited a specific surface area of 14 m^2 g^{-1}, the former presented a pore volume twice as large as the latter. As will be shown later, this was because the pores in the CC sample were significantly larger than in the SCS oxide, thereby occupying a larger volume for the same specific surface area.

Table 1. Textural and structural properties of the bulk Co_3O_4 catalysts.

| Catalyst	BET Surface, m^2 g^{-1}	Pore Volume, cm^3 g^{-1}	Mean Pore Diameter, Å	Crystallite Size, nm	Cell Parameter, Å
DC	5	0.02	355	84	8.09844 ± 0.00018
HC	12	0.06	350	64	8.09887 ± 0.00016
GB	16	0.10	275	58	8.09899 ± 0.00019
CN	6	0.02	460	92	8.09879 ± 0.00016
CC	14	0.09	255	63	8.09908 ± 0.00015
OW	9	0.02	170	86	8.09861 ± 0.00015
SCS	14	0.04	170	89	8.09884 ± 0.00012
SG	5	0.01	370	102	8.09854 ± 0.00016
COM	8	0.03	410	75	8.09883 ± 0.00016

The average pore diameter of the catalysts varied from 170 Å for the OW and SCS samples to 460 Å for the CN sample. A detailed inspection of the pore size distributions, included in Figure 1, revealed some differences between the prevalent pore diameter and the mean pore diameter of various samples. Firstly, although both OW and SCS samples exhibited a mean pore size of 170 Å, their respective pore size distributions were notably different. The SCS sample presented a bimodal distribution with maxima around 90 and 700 Å, while the OW sample was characterized by a relatively homogeneous distribution with a relatively small maximum at around 800 Å. In addition, the SG sample displayed a pore size distribution very similar to that of the OW sample, with a small maximum at around 1090 Å. Nevertheless, their respective mean pore sizes were notably different (370 and 170 Å, respectively). Several samples exhibited pore size distributions with marked maxima in somewhat comparable values. In particular, the CC, GB, HC and DC oxides revealed unimodal distributions centered in the mesopore region. The CC and GB samples revealed analogous distributions centered around 335 Å, in agreement with their akin mean pore diameter (255–275 Å). In this sense, the HC and DC samples also presented almost equivalent mean pore sizes (350 Å) in line with their comparable size distributions, although the former exhibited a larger pore volume.

The structural properties of the bulk catalysts were investigated by XRD. Figure S2, Supplementary material includes the diffractograms of the nine samples. All catalysts exhibited the expected pattern of a cubic phase of Co_3O_4 (ICDD 00-042-1467). No diffraction signals from other cobalt phases such as CoO or metallic Co were detected. The average Co_3O_4 crystallite size (Table 1) was estimated by the application of the Scherrer equation with the full width half maximum of the most intense signal of the spinel, located at 2θ = 36.8° and corresponding to the (3 1 1) plane. The crystallite size varied from 58–64 nm for the GB, CC and HC samples to 102 nm for the SG sample. A relatively clear inverse relationship was found between the textural properties and the structural properties in terms of crystallite size. This was expected since smaller crystallites tend to exhibit larger available surface areas [19,20].
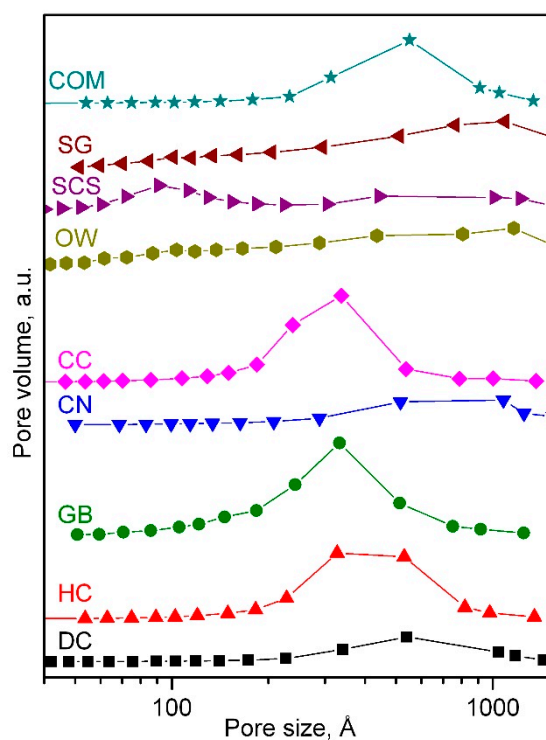
**Figure 1.** Pore size distributions of the bulk Co_3O_4 catalysts.

Despite all samples exhibiting the same diffraction signals, their relative position significantly varied among the synthesized catalysts. Thus, a close-up view of the most intense signal (Figure 2) pointed out that its position varied between 37.05° for the CC, GB and COM samples, up to 37.12° for the SG, SCS and OW samples. This variation in the relative position of the diffraction signals implied slight differences in the cell parameter of the Co_3O_4 spinel lattice (Table 1), with the catalysts with signals centered at lower diffraction angles having larger cell parameters with respect to those oxides with signals located at higher angles [21,22]. This behavior could be due to some degree of structural distortion in their crystalline lattice.
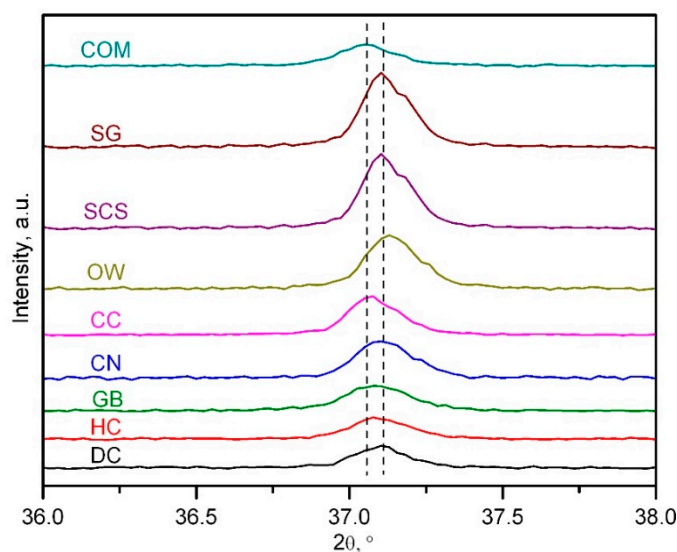
Figure 2. Close-up view of the XRD patterns of the bulk Co_3O_4 catalysts in the 36–38° range.

This distortion could be also evidenced by the analysis of the Raman spectra of the catalysts (Figure S3, Supplementary Material). As expected, the spectra of all the synthesized catalysts exhibited the five vibration modes characteristic of the Co_3O_4 spinel: three F_{2g} modes centered at 194 (not shown), 525 and 620 cm^{-1}, one E_g mode at 479 cm^{-1} and one A_{1g} mode at around 688 cm^{-1} [23]. This last vibration mode, which was the most intense for Co_3O_4 samples, presented varying width and asymmetry depending on the used synthesis route. Hence, in most samples, two distinct contributions could be observed, namely one centered at 685 cm^{-1} and the other one located at 700 cm^{-1}.

The shift of the peak position to lower wavenumbers is an indication of a distorted lattice characterized by the abundance of crystal defects giving rise to oxygen vacancies that can be beneficial for the activation of oxygen molecules to active oxygen species [24]. Thus, the relative intensity of the vibration modes at 685 and 700 cm^{-1} (I_{700}/I_{685}), which was significantly different for the investigated oxides, could be employed as a criterion for comparing the extent of lattice distortion of each Co_3O_4 sample. Accordingly, more distorted lattices would show larger cell parameters. Results included in Figure 3 pointed out a relatively good consistency of the data extracted from both XRD and Raman spectroscopy, and this suggested that the crystalline structure of CC, GB and COM samples was comparatively more defective with I_{700}/I_{685} ratios (<0.1) and large cell parameter (8.09899–8.09908 Å), while fewer defects should be expected for the OW, SG and DC oxides.
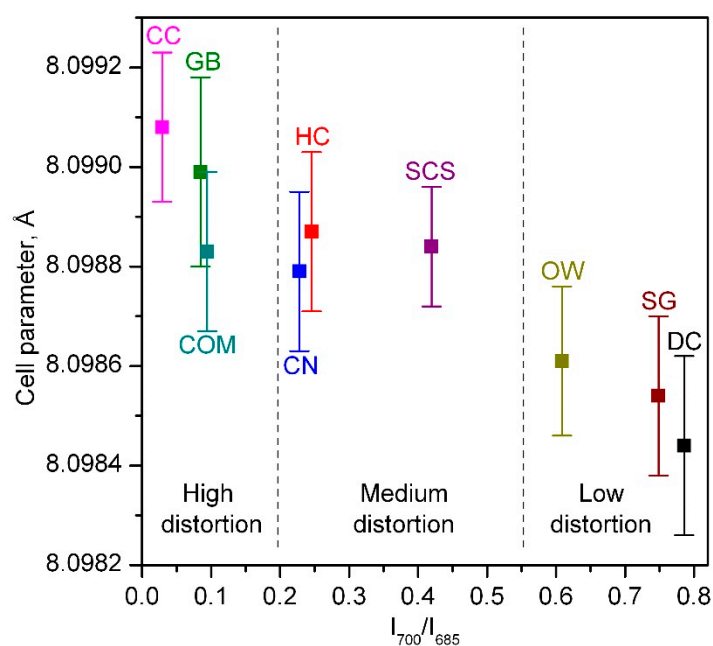
Figure 3. Evolution of the lattice distortion of the bulk Co_3O_4 catalysts.

The surface composition of the bulk Co_3O_4 samples was investigated by deconvolution and integration of the XPS $Co2p_{3/2}$ and O1s spectra (Figure 4). Firstly, the $Co2p_{3/2}$ was deconvoluted into five contributions, which corresponded to three main signals and two satellites. Thus, the signals located at 779.5 and 780.8 eV were attributed to the presence of Co^{3+} and Co^{2+} ions, respectively, while the third main signal, centered at around 782.1 eV, was associated with the existence of Co^{2+} as CoO [25]. This latter signal is generally assumed to be formed due to partial surface reduction of the Co_3O_4 samples after being exposed to the vacuum conditions of the XPS apparatus. Finally, the signals located at 785.5 and 789.5 eV were identified as the shake-up satellite signals from the Co^{2+} and Co^{3+} ions, respectively [26]. On the other hand, the O1s spectra of the samples was deconvoluted into four signals located at 529.5, 530.6, 531.5 and 532.6 eV, which were identified as lattice oxygen species, adsorbed oxygen species, oxygen from carbonate and hydroxyl groups and oxygen from adsorbed water, respectively [27,28].
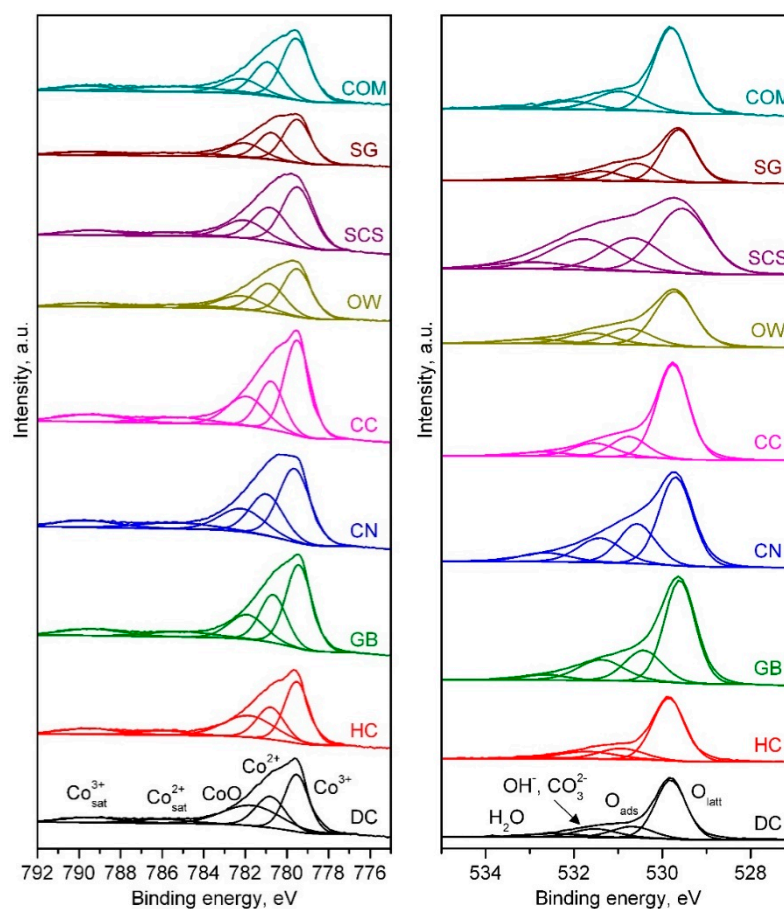
**Figure 4.** Co2p$_{2/3}$ (**left**) and O1s (**right**) XPS spectra of the bulk Co$_3$O$_4$ catalysts.

The surface composition in terms of Co^{3+}/Co^{2+} and O$_{ads}$/O$_{latt}$ molar ratios estimated from the aforementioned deconvolutions is summarized in Table 2. These results suggested an inverse correlation between these two ratios, with the presence of Co^{3+} ions in the catalysts being related to a higher abundance of lattice oxygen species [29,30]. Among all the samples, the CC, GB and COM catalysts, which were characterized by a marked lattice distortion judging from the results from both XRD and Raman spectroscopy, evidenced the most favored presence of Co^{3+} ions on their surface.

Table 2. Surface composition of the bulk Co$_3$O$_4$ catalysts.

Catalyst	Co^{3+}/Co^{2+} Molar Ratio	O$_{ads}$/O$_{latt}$ Molar Ratio
DC	1.50	0.57
HC	1.70	0.49
GB	1.73	0.45
CN	1.69	0.49
CC	1.96	0.40
OW	1.52	0.57
SCS	1.65	0.57
SG	1.60	0.53
COM	1.76	0.45

The reducibility of the synthesized oxides was investigated by means of the H$_2$-TPR technique. The corresponding reduction profiles are depicted in Figure 5. All reduction profiles presented a two-step reduction process, although their characteristic reduction temperatures varied considerably. The first reduction event, peaking at between 300 and 330 °C, corresponded to the reduction of Co^{3+} cations into Co^{2+} (Equation (1)), while the

second one, located at around 350–400 °C, was attributed to the reduction of the Co^{2+} cations to metallic cobalt Co^0 (Equation (2)) [31,32]. This second reduction process often occurred in a relatively wide temperature window, and several different contributions could be identified, thus suggesting the presence of various types of Co^{2+} species with various degrees of reducibility. No additional hydrogen uptakes were detected above 500 °C. It was therefore concluded that the only reducible phase in the samples was Co_3O_4.

$$Co_3O_4 + H_2 \ \rightarrow \ 3CoO + H_2O \tag{1}$$

$$3CoO + 3H_2 \ \rightarrow \ 3Co + 3H_2O \tag{2}$$
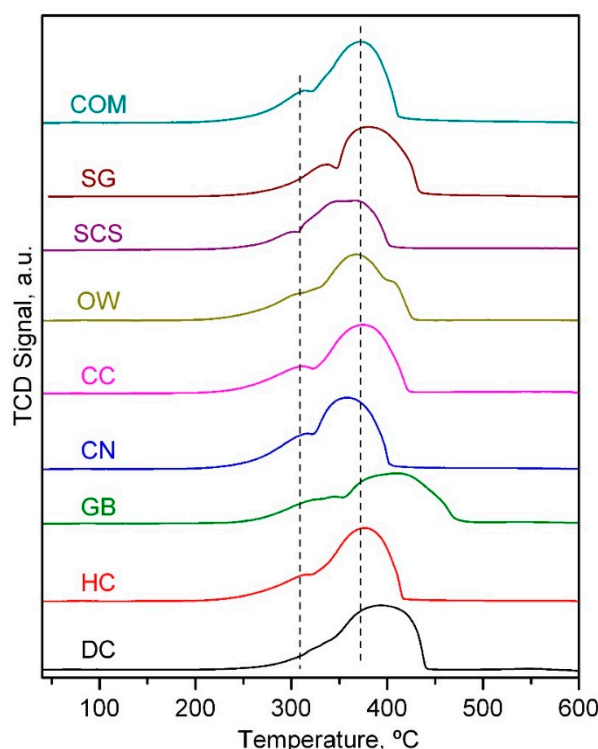
Figure 5. H_2-TPR profiles of the bulk Co_3O_4 catalysts.

After integration and quantitative evaluation of the TPR profiles, the specific hydrogen uptake of each reduction step and the corresponding ratio were computed, as shown in Table 3. In all cases, the total amount of hydrogen consumed during the process was close to 16.6 mmol g^{-1}, which coincided with the stoichiometric amount required for the complete reduction of Co_3O_4. Ideally, the relative H_2 uptake between the low-temperature and high-temperature contributions would be 0.33. However, this ratio varied between 0.19 for the DC sample to 0.38 for the CC sample. This revealed marked differences in reducibility and relative distribution of the reducible species (Co^{3+} and Co^{2+} species) with the used synthesis methodology.

Moreover, the temperature for the onset of reduction, defined as the temperature at which 5% of the total H_2 uptake was consumed, also evidenced substantial variations. Hence, the onset temperature shifted from 265 °C for the CC catalyst to 300 °C for the DC sample. The onset temperature could be correlated with the aforementioned ratio between low- and high-temperature uptakes, since the samples that started to be reduced at lower temperatures also tended to consume larger H_2 amounts at low temperatures. However, this trend was not fully consistent for all the samples, since the onset temperature was also notably influenced by the textural and structural properties of the samples.

Table 3. Results of the H_2-TPR analysis of the bulk Co_3O_4 catalysts.

Catalyst	Low-Temperature H_2 Uptake, mmol g^{-1}	High-Temperature H_2 Uptake, mmol g^{-1}	Relative H_2 Uptake at Low and High Temperature	Onset Reduction Temperature, °C
DC	2.6	13.9	0.19	300
HC	3.3	13.4	0.25	270
GB	4.3	12.4	0.34	285
CN	4.1	12.6	0.32	270
CC	4.6	12.0	0.38	265
OW	3.4	12.3	0.25	270
SCS	3.9	12.7	0.30	280
SG	4.0	12.7	0.32	290
COM	4.2	12.4	0.34	275

The analysis by H_2-TPR allowed for the calculation of the degree of reducibility of the samples, which was presumed a key catalytic property for oxidative applications [33–35], to be estimated. On one hand, various samples, namely the CC, GB, CN and COM oxides, exhibited relatively high H_2 uptakes at low temperatures (4.1–4.5 mmol H_2 g^{-1}) with low onset temperatures (265–285 °C), thus showing a high reducibility. On the other hand, the DC, OW and HC samples were characterized by relative uptakes at low and high temperatures (0.19–0.25) well below the stoichiometric value (0.33), and considerably higher onset temperatures (270–300 °C), thereby exhibiting a poorer reducibility.

Despite the investigation of the redox properties of the bulk Co_3O_4 catalysts by H_2-TPR revealed some differences among the various samples, a complementary analysis was made by substituting H_2 by CH_4. This change of the reducing agent was expected to provide more realistic insights on the reactive available oxygen species for methane oxidation. The exit stream of these new CH_4-TPRe experiments was analyzed by mass spectrometry, following the evolution of the $m/z = 44$ (CO_2) signal with the temperature (Figure S4, Supplementary material). For most of the samples, the formation of CO_2 was noticeable at two different temperature windows: 350–550 °C and 550–600 °C. The observed CO_2 generation at lower temperatures was attributed to the oxidation of methane by oxygen species associated with Co^{3+} ions, while, at higher temperatures, the CO_2 production was assigned to the oxidation of methane by oxygen species associated with Co^{2+} ions [36]. Indeed, most valuable data could be extracted from the detected production of CO_2 at lower temperatures, since this corresponded to the full oxidation of methane by the active oxygen species of the bulk Co_3O_4 catalysts. Therefore, a close-up view of the CO_2 generation profiles in the 300–550 °C temperature window is included in Figure 6.

It was observed that the reactivity of the oxygen species varied significantly with the synthesis methodology, on account of the different peak temperatures exhibited by each catalyst, which were in the 485–510 °C range. The catalysts with the lowest peak temperatures were the CC (485 °C), GB (492 °C), COM and HC (495 °C), while the ones with the highest peak temperatures were the OW (501 °C) and SG (509 °C) samples. Simultaneously, the O_2 consumption derived from that low-temperature CO_2 generation profiles decreased from 0.33 mmol g_{Co}^{-1} for the CC catalyst, to 0.16 mmol g_{Co}^{-1} for the DC, OW and SCS samples, thus revealing that not only the intrinsic reactivity, but also the amount of active oxygen species of the bulk Co_3O_4 catalysts was highly dependent on its synthesis route.
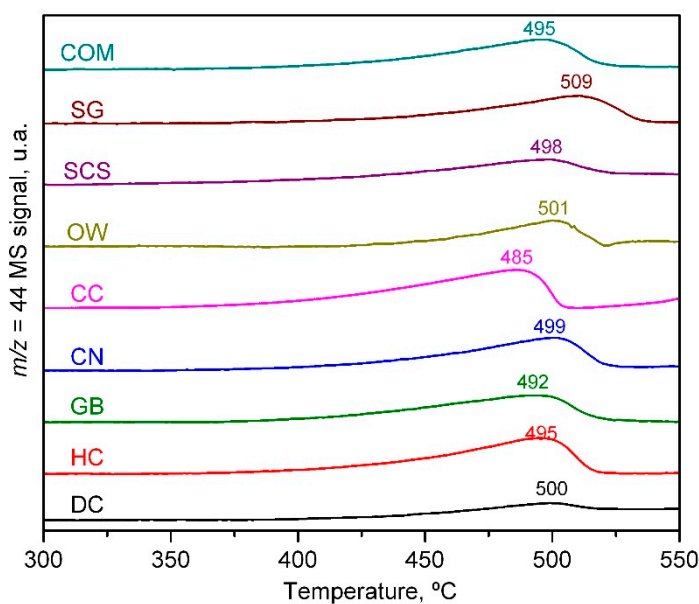
Figure 6. CH_4-TPRe profiles of the bulk Co_3O_4 catalysts in the low-temperature range (300–500 °C).

2.2. Catalytic Performance of the Synthesised Catalysts

The catalytic efficiency of bulk Co_3O_4 catalysts for the complete oxidation of lean methane was evaluating by obtaining their respective light-off curves at 60,000 h^{-1}. These light-off curves were recorded between 200 °C and the calcination temperature of the catalysts (600 °C). For each sample, three consecutive tests were performed and the data from the third cycle was taken as the characteristic curve for a given catalyst (Figure 7), since, in all cases, the second and third cycles were identical. To ensure that the obtained kinetic results with powdered catalysts were not affected by mass or heat transfer limitations, the criteria for intra-particle and extra-particle mass and energy diffusion, as well as the temperature gradients were checked. In this sense, Table S1, Supplementary Material lists the calculated values for the various evaluated criteria over the CC catalyst.
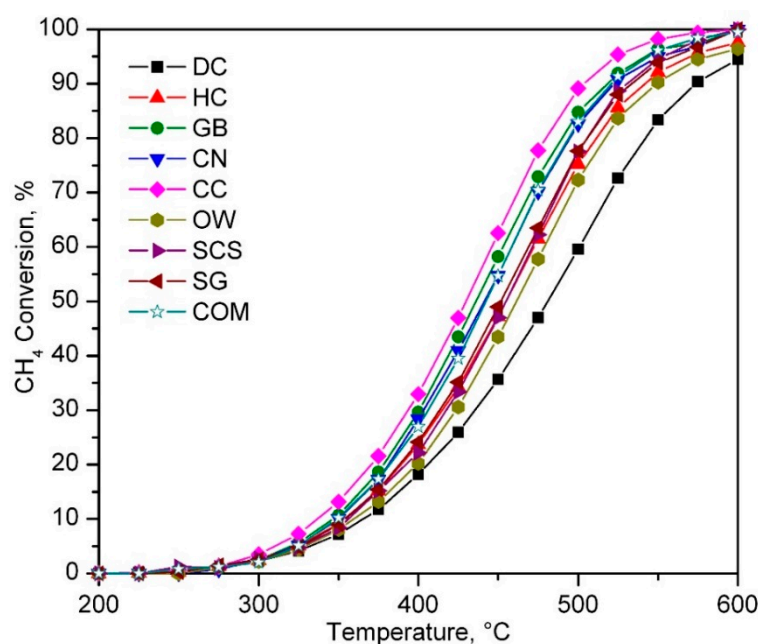
Figure 7. Light-off curves of the bulk Co_3O_4 catalysts.

All synthesized catalysts exhibited a 100% selectivity towards CO_2 formation. Based on the T_{50} values (temperature required to achieve 50% CH_4 conversion), the following trend was found: CC > GB > CN > COM > SG > SCS > HC > OW > DC. Interestingly, the bulk oxides that achieved the lowest T_{50} values were those that presented a promoted reducibility, according to the H_2-TPR results, which, in turn, was coherent with the marked distortion of their lattice and abundant of oxygen vacancies as pointed out by XRD and Raman spectroscopy.
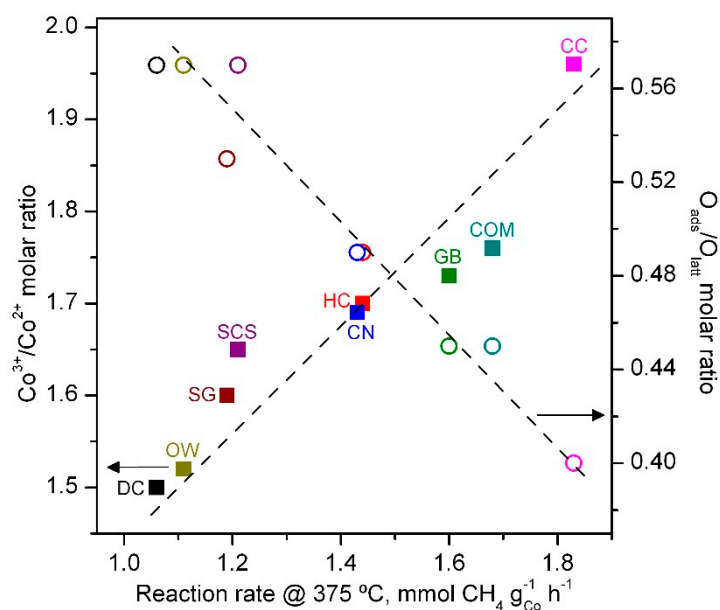
The specific reaction rate of the catalysts was estimated at 375 °C under differential conditions, that is, for methane conversions lower than 20%. The calculated values were in the 1.06–1.83 mmol CH_4 g_{Co}^{-1} h^{-1} range (Table 4). The CC catalyst exhibited the highest specific activity, followed by the COM (1.68 mmol CH_4 g_{Co}^{-1} h^{-1}) and the GB (1.60 mmol CH_4 g_{Co}^{-1} h^{-1}) catalysts. In contrast, the DC (1.06 mmol CH_4 g_{Co}^{-1} h^{-1}) and OW (1.11 mmol CH_4 g_{Co}^{-1} h^{-1}) samples achieved the slowest reaction rates. While assuming a first-order for methane and a zeroth pseudo order for oxygen, the apparent activation energy of all synthesized samples was quite similar (71–75 kJ mol^{-1}), and reasonably comparable with the values reported in the literature for methane oxidation over cobalt oxide catalysts [37–39].

**Table 4.** Kinetic results of the bulk Co_3O_4 catalysts.

Catalyst	T_{50}, °C	Reaction Rate at 375 °C, mmol CH_4 g_{Co}^{-1} h^{-1}	Ea, kJ mol^{-1}
DC	480	1.06	71 ± 2
HC	455	1.44	74 ± 2
GB	435	1.60	74 ± 1
CN	440	1.43	74 ± 2
CC	430	1.83	74 ± 2
OW	460	1.11	73 ± 2
SCS	455	1.21	75 ± 1
SG	450	1.19	73 ± 2
COM	440	1.68	74 ± 1

The activity of the synthesized bulk Co_3O_4 catalysts seemed to find its origin in the presence of Co^{3+} ions found on their surface according to the strong correlation found between the molar Co^{3+}/Co^{2+} ratio from the XPS analysis and the calculated reaction rate, which is shown in Figure 8. Recall that the molar Co^{3+}/Co^{2+} ratio was in turn inversely correlated to the O_{ads}/O_{latt} molar ratio. Accordingly, the reaction rate of the samples was controlled by the abundance of lattice oxygen species on their surface.

The key role played by oxygen species was also evidenced by the observed strong correlation between the reaction rate and the O_2 consumption at low temperature estimated from the CH_4-TPRe runs, as shown in Figure 9. This relationship would be in agreement with the Mars—van Krevelen mechanism, which is commonly accepted for lean methane oxidation [40], since the catalysts that exhibited larger O_2 consumption due to their favored mobility of oxygen species exhibited a higher catalytic activity. In this sense, the CC methodology seemed to be able to optimize the abundance of Co^{3+} ions on the surface of the prepared Co_3O_4 catalyst, which in turn resulted in a more abundant presence of lattice oxygen species with high mobility, as evidenced by the aforementioned correlations depicted in Figure 8.

Figure 8. Relationship between reaction rate and the surface composition, in terms of Co^{3+}/Co^{2+} and O_{ads}/O_{latt} molar ratios, of the bulk Co_3O_4 catalysts.
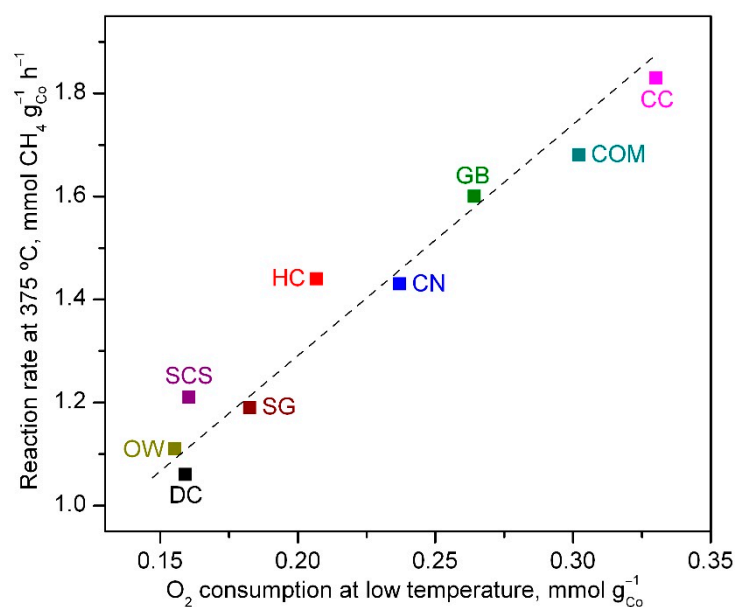
Figure 9. Relationship between reaction rate and the specific O_2 consumption at low temperature derived from the CH_4-TPRe runs.

Finally, the stability with time on stream of the most active catalyst, namely the sample synthesized following the CC route, was investigated under dry and humid (10%vol.) conditions under isothermal conditions (500 °C) for a total reaction time of 150 h. The evolution of the methane conversion during this run is shown in Figure 10. During the first 25 h of time on stream, the catalyst gave a reasonably constant conversion at around 89%, thus exhibiting a notable thermal stability with no apparent evidence of deactivation. Upon the admission of water vapor to the feedstream, a significant decrease to a stable value of 70% was then observed. Interestingly, when water was subsequently cut off, the methane conversion was almost fully recovered, attaining a value similar (88%) to that observed under dry conditions. Hence, it was evidenced that the inhibiting effect of water due to coverage of the active sites was essentially temporary and did not lead to

any significant irreversible catalyst deactivation. The conversion pattern during the two consecutive dry/humid cycles reflected a virtually identical behavior.
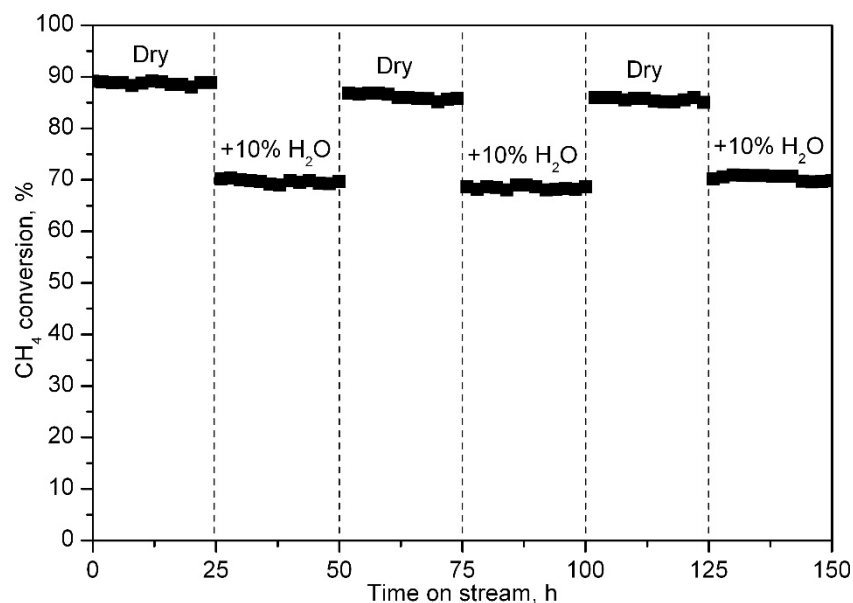
Figure 10. Evolution of methane conversion with time on stream over the CC catalyst under alternating dry/humid conditions at 500 °C.

After this stability test, the used catalyst was characterized in order to determine any possible detrimental effect that the exposure to water vapor could have had on the catalyst. On one hand, the N_2 physisorption analysis evidenced a slight decrease in the specific surface area (from 14 to 12 m^2 g^{-1}), in agreement with the small enlargement of the Co_3O_4 crystallite size (from 63 to 70 nm) uncovered by XRD. On the other hand, the CH_4-TPRe profile of the used catalyst presented a slight shift of the peak temperature (495 °C) with respect to the fresh counterpart (485 °C), as shown in Figure S5 (Supplementary material), although the O_2 consumption at low temperature was hardly altered (0.31 mmol g_{Co}^{-1} for both fresh and used oxides). These results suggested that the spent catalyst had not suffered any significant loss in the redox properties apart from those caused by the slight sintering of the Co_3O_4 crystallites.

3. Materials and Methods

3.1. Synthesis of the Bulk Catalysts

Firstly, the two methodologies based on direct calcination implied a simple thermal activation in static air in a muffle oven of a given cobalt salt. Particularly, certain amounts of cobalt (II) nitrate hexahydrate (around 18 g, $Co(NO_3)_2 \cdot 6H_2O$, Honeywell Fluka, Morristown, NJ, USA) and cobalt hydroxycarbonate (about 6.5 g, $Co_2CO_3(OH)_2$, Panreac, Barcelona, Spain) were calcined, leading to the so-called DC and HC samples, respectively.
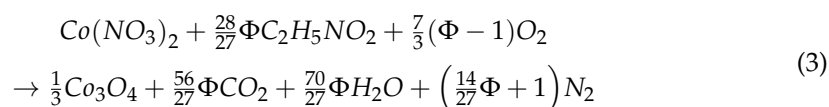
The reactive basic grinding (GB) synthesis route involved grinding a mixture of 9 g of cobalt (II) nitrate hexahydrate and 6.1 g of ammonium hydrogen carbonate ($(NH_4)HCO_3$, Honeywell Fluka, Morristown, NJ, USA) in an agate mortar for 30 min. The mixture behaved like a heterogeneous physical mixture for the first minutes of grinding. Afterwards, the two components started reacting between themselves to produce a homogeneous paste that was later dried and subjected to calcination.

Regarding the precipitation methodologies, three different approaches were investigated, although the common experimental protocol was similar. In the three cases, a 100 cm^3 aqueous solution of cobalt nitrate (II) hexahydrate was placed in the synthesis reactor and heated to 80 °C. Then, the precipitation of a cobalt precursor was induced by the dropwise addition of a precipitating agent, until the pH reached 8.5. After their

respective precipitation processes, each solid was filtered and thoroughly washed with, at least, 8 L of deionized hot water. The precipitates were then dried in static air at 110 °C for 16 h and submitted to calcination to form the final catalysts.

As for the CN catalyst, the precipitating agent was a solution of ammonium carbonate 1 M, while a solution of sodium carbonate 1.2 M was used for the CC sample. Finally, in the case of the OW sample the precipitating agent was an aqueous solution of NaOH 3.2 M. Once the precipitation was complete, 100 cm^3 of 50% H_2O_2/50% H_2O (Sigma Aldrich, Darmstadt, Germany) were added dropwise to the reaction mixture.

The solution combustion synthesis (SCS) route involved the flameless combustion of an organic fuel (glycine) with an oxidizer (cobalt (II) nitrate hexahydrate), which generated the energy necessary to transform the cobalt species into cobalt oxide. The synthesis methodology consisted of preparing a solution (50 cm^3) of the cobalt salt and glycine. A small volume of this solution (around 2 cm^3) was placed inside a muffle oven, where it was first heated at 250 °C for 30 min and then subjected to calcination. The stoichiometric concentrations of glycine and cobalt nitrate were chosen for the complete combustion of the fuel and nitrates into CO_2, H_2O and N_2, as shown in Equation (3):

$$Co(NO_3)_2 + \frac{28}{27}\Phi C_2H_5NO_2 + \frac{7}{3}(\Phi - 1)O_2$$
$$\rightarrow \frac{1}{3}Co_3O_4 + \frac{56}{27}\Phi CO_2 + \frac{70}{27}\Phi H_2O + \left(\frac{14}{27}\Phi + 1\right)N_2 \tag{3}$$

Finally, the sol-gel (SG) approach was based on the complexation of cobalt (II) nitrate hexahydrate with citric acid. Thus, 3.5 g of citric acid were added to 250 cm^3 of a solution of the cobalt salt 0.1 M. The solution was heated to 40 °C to progressively evaporate the water until the formation of a viscous gel. The gel was subsequently placed in a drier at 70 °C to further evaporate the remaining water during 16 h. The result was a spongy, highly hygroscopic material that was crushed and calcined in a muffle oven.

All cobalt catalytic precursors, including the commercial sample (COM), were calcined in static air as the last step of each specific synthesis route. The calcination protocol was defined in view of the results obtained from a previous thermogravimetric analysis performed over cobalt hydroxycarbonate selected as a reference precursor. This experiment involved three heating steps separated by 30-min isotherms: a first one from ambient temperature to 125 °C, a second one from 125 to 300 °C and the last one from 300 to 600 °C.

3.2. Characterisation Techniques

The textural properties, in terms of BET surface area, pore volume and average pore diameter, were measured by nitrogen physisorption at 77 K in a Micromeritics Tristar II (Micromeritics Instrument Corp., Norcross, GA, USA) apparatus. All samples were subjected to degassing prior to the analysis at 300 °C for 10 h with a N_2 flow in a Micromeritics SmartPrep (Micromeritics Instrument Corp., Norcross, GA, USA) degasser. The pore size distributions were calculated from the data provided by the desorption step by using the BJH method.

The structure of the synthesized catalysts was investigated by XRD and Raman spectroscopy. X-ray diffraction (XRD) analysis were carried out on a X'PERT-PRO X-ray diffractometer (Malvern Panalytical, Malvern, UK) using Cu Kα radiation (λ = 1.5406 Å) and a Ni filter. The X-ray emitter was operated at 40 kV and 40 mA. The diffractograms were recorded in the 2θ = 5–80° range with a step size of 0.026°. The Raman spectra of the samples were obtained with a Renishaw InVia Raman Spectrometer (Renishaw plc, Wotton-under-Edge, UK) coupled to a Leica DMLM microscope (Leica Microsystems, Wetzlar, Germany). For each spectrum, 20 s were employed and five scans were accumulated with a 514 nm laser at 10% of its maximum power. The spectra were registered in the spectra window of 150–1500 cm^{-1}.

The surface composition of the samples was studied by X-ray photoelectron spectroscopy (XPS). The XPS spectra were obtained using a SPECS system coupled with a Phoibos 150 1D analyzer (SPECS GmbH, Berlin, Germany) and a DLD monochromatic

radiation source. The registered spectra were corrected by fixing the signal of the C1s spectra assigned to the adventitious carbon to a binding energy of 284.6 eV.

The redox properties of the catalysts were measured by H_2-TPR and CH_4-TPRe. Both analysis were carried out in a Micromeritics Autochem 2920 (Micromeritics Instrument Corp., Norcross, GA, USA) apparatus. For the H_2-TPR analysis, the reducing agent was 5% H_2/Ar gaseous mixture while for the CH_4-TPRe it was a 5% CH_4/He mixture. All experiments were carried out from ambient temperature up to 600 °C with a 30-min isotherm at 600 °C. The output stream from the H_2-TPR experiments was analyzed by a TCD while the one from the CH_4-TPRe experiment was analyzed with a MKS Cirrus Quadrupole Mass Spectrometer (MKS Instruments, Andover, MA, USA).

3.3. Evaluation of the Catalytic Activity and Stability

The catalytic activity and stability of the synthesized catalysts was evaluated in a PID Eng&Tech MICROACTIVITY Reference (Process Integral Development S.L., Alcobendas, Spain) bench scale reactor at atmospheric pressure. The equipment consisted on a fixed bed tubular reactor placed inside an oven controlled by a thermocouple inserted into the catalytic bed. For each experiment, 1 g of catalyst, in the form of 0.25–0.3 mm particles, was diluted with 1 g of inert quartz (0.5–0.8 mm) and placed into the reactor tube. The activity experiments were carried out from 200 to 600 °C with a feedstream composed of 1% CH_4, 10% O_2 and 89% N_2, fed with a total flow rate of 500 cm^3 min^{-1}, which corresponded to a GHSV of 60,000 h^{-1}. On the other hand, the stability tests were carried out by feeding the aforementioned gaseous mixture at a constant temperature of 500 °C during 25 h, after which water vapor (10%vol.) was added for an additional 25 h. The 10%vol. of water vapor was fed to the reactor as liquid water via an alternative liquid pump. The liquid water was pumped to an evaporator that was kept at 150 °C in order to ensure the complete vaporization of the water before mixing it with the rest of the gaseous feedstream. This cycle was repeated two more times for a total accumulated reaction time of 150 h. The analysis of the outlet stream from the reactor was carried out with an Agilent Technologies MicroGC (Agilent Technologies, Santa Clara, CA, USA) equipped with a TCD. Methane conversion was calculated by measuring the differences in concentration between the inlet and the outlet streams.

4. Conclusions

Several bulk Co_3O_4 catalysts were prepared by following various synthesis methodologies and examined for the complete methane oxidation reaction in order to assess the effect of the synthesis route on their physico-chemical properties and efficiency in the oxidation of lean methane.

All synthesized catalysts were characterized by a relatively low specific surface area and large crystallite sizes, as expected for bulk oxides. Among the studied synthesis methodologies, the solution combustion synthesis route (SCS), the basic grinding route (GB), the calcination of cobalt hydroxycarbonate route (HC) and the precipitation with sodium carbonate route (CC), seemed to be able to obtain better textural properties than the commercial catalyst. Except from the SCS oxide, these samples also exhibited crystallites sizes smaller than that of the reference sample. Furthermore, CC and GB catalysts were characterized by a notable lattice distortion, which in principle would lead to the greater abundance of oxygen vacancies.

The surface composition of the catalysts was strongly dependent on the synthesis methodology, with the relative Co^{3+} abundance varying significantly among the studied samples and being somewhat related to the optimization of the textural and structural properties. In this sense, the three aforementioned catalysts (CC, GB and HC), along with the commercial sample exhibited a higher presence of Co^{3+} ions on their surface. This, in turn, resulted in an increased abundance of lattice oxygen species, with the CC catalyst exhibiting the highest amount. The redox properties of the synthesized catalysts were generally coherent with these findings, since the oxides that showed the highest amounts

of Co^{3+} on their surface were more reducible and exhibited higher H_2 uptakes and O_2 consumptions at low temperatures as well. Hence, it was demonstrated that the amount and reactivity of the active lattice oxygen species in the structure of the Co_3O_4 catalysts depends mainly on the abundance of Co^{3+}. In this sense, in line with the results from XPS, the catalyst prepared with the CC route exhibited the best redox properties. These best redox properties made this catalyst the most active among all studied catalysts. In addition to that, this bulk oxide evidenced a notable thermal stability over prolonged periods. The addition of water vapor to the reaction mixture seemed to partially inhibit the catalyst activity, but no significant irreversible deactivation was found.

Supplementary Materials: The following supporting information can be downloaded at: https://www.mdpi.com/article/10.3390/catal12010087/s1, Table S1: Criteria for accurate analysis of intrinsic reaction rates of the foam catalysts (as estimated for the CC catalyst at 375 °C), Figure S1: N_2 physisorption isotherms of the bulk Co_3O_4 catalysts, Figure S2: XRD patterns of the bulk Co_3O_4 catalysts, Figure S3: Raman spectra of the bulk Co_3O_4 catalysts, Figure S4: CH_4-TPRe profiles of the bulk Co_3O_4 catalysts, Figure S5: Close-up view of the CH_4-TPRe profiles in the 300–500 °C range of the CC catalyst before and after the stability test.

References

1. Raj, A. Methane emission control. *Johns. Matthey Technol. Rev.* **2016**, *60*, 228–235. [CrossRef]
2. Khan, M.I.; Yasmin, T.; Shakoor, A. Technical overview of compressed natural gas (CNG) as a transportation fuel. *Renew. Sust. Energ. Rev.* **2015**, *51*, 785–797. [CrossRef]
3. Huang, S.; Li, T.; Wang, X.; Chen, R.; Yang, R.; Qian, Z. Effects of various discharge strategies on ignition and combustion of lean natural gas mixture under the static and turbulent conditions. *Exp. Therm. Fluid Sci.* **2022**, *133*, 110581. [CrossRef]
4. Wang, J.; Gui, H.; Yang, Z.; Yu, T.; Zhang, X.; Liu, J. Real-world gaseous emission characteristics of natural gas heavy-duty sanitation trucks. *J. Environ. Sci.* **2022**, *115*, 319–329. [CrossRef]
5. Maunula, T.; Kallinen, K.; Kinnunen, N.; Keenan, M.; Wolff, T. Methane abatement and catalyst durability in heterogeneous lean-rich and dual-fuel conditions. *Top. Catal.* **2019**, *62*, 315–323. [CrossRef]
6. Kinnunen, N.M.; Hirvi, J.T.; Kallinen, K.; Maunula, T.; Keenan, M.; Suvanto, M. Case study of a modern lean-burn methane combustion catalyst for automotive applications: What are the deactivation and regeneration mechanisms? *Appl. Catal. B Environ.* **2017**, *207*, 114–119. [CrossRef]
7. Velin, P.; Ek, M.; Skoglundh, M.; Schaefer, A.; Raj, A.; Thompsett, D.; Smedler, G.; Carlsson, P.-A. Water inhibition in methane oxidation over alumina supported palladium catalysts. *J. Phys. Chem. C* **2019**, *123*, 25724–25737. [CrossRef]
8. Mihai, O.; Smedler, G.; Nylén, U.; Olofsson, M.; Olsson, L. The effect of water on methane oxidation over Pd/Al_2O_3 under lean, stoichiometric and rich conditions. *Catal. Sci. Technol.* **2017**, *7*, 3084–3096. [CrossRef]
9. Tang, W.; Weng, J.; Lu, X.; Wen, L.; Suburamanian, A.; Nam, C.-Y.; Gao, P.-X. Alkali-metal poisoning effect of total CO and propane oxidation over Co_3O_4 nanocatalysts. *Appl. Catal. B Environ.* **2019**, *256*, 117859. [CrossRef]
10. González-Prior, J.; López-Fonseca, R.; Gutiérrez-Ortiz, J.I.; de Rivas, B. Catalytic removal of chlorinated compounds over ordered mesoporous cobalt oxides synthesised by hard-templating. *Appl. Catal. B Environ.* **2018**, *222*, 9–17. [CrossRef]
11. Ma, Z. Cobalt oxide catalysts for environmental remediation. *Curr. Catal.* **2014**, *3*, 15–26. [CrossRef]

12. Setiawan, A.; Kennedy, E.M.; Dlugogorski, B.Z.; Adesina, A.A.; Stockenhuber, M. The stability of Co_3O_4, Fe_2O_3, Au/Co_3O_4 and Au/Fe_2O_3 catalysts in the catalytic combustion of lean methane mixtures in the presence of water. *Catal. Today* **2015**, *258*, 276–283. [CrossRef]

13. Zhang, W.; Descorme, C.; Valverde, J.L.; Giroir-Fendler, A. Cu-Co mixed oxide catalysts for the total oxidation of toluene and propane. *Catal. Today* **2022**, *384–386*, 238–245. [CrossRef]

14. Karthick, S.N.; Hemalatha, K.V.; Justin Raj, C.; Kim, H.J.; Yi, M. Synthesis of nano-bound microsphere Co_3O_4 by simple polymer-assisted sol-gel technique. *J. Nanopart. Res.* **2013**, *15*, 1474. [CrossRef]

15. Arango-Diaz, A.; Cecilia, J.A.; Marrero-Jerez, J.; Nuñez, P.; Jiménez-Jiménez, J.; Rodríguez-Castellón, E. Freeze-dried Co_3O_4-CeO_2 catalysts for the preferential oxidation of CO with the presence of CO_2 and H_2O in the feed. *Ceram. Int.* **2016**, *42*, 7462–7474. [CrossRef]

16. Ercolino, G.; Stelmachowski, P.; Specchia, S. Catalytic performance of Pd/Co_3O_4 on SiC and ZrO_2 open cell foams for process intensification of methane combustion in lean conditions. *Ind. Eng. Chem. Res.* **2017**, *56*, 6625–6636. [CrossRef]

17. Wang, Q.; Deng, W.; Lin, X.; Huang, X.; Wei, L.; Gong, L.; Liu, C.; Liu, G.; Liu, Q. Solid-state preparation of mesoporous Ce–Mn–Co ternary mixed oxide nanoparticles for catalytic degradation of methylene blue. *J. Rare Earth.* **2021**, *39*, 826–834. [CrossRef]

18. Liu, B.; Peng, J.; Zhang, L.; Wan, R.; Guo, S.; Zhou, L. Optimization of preparation for Co_3O_4 by calcination from cobalt oxalate using response surface methodology. *Chem. Eng. Res. Des.* **2010**, *88*, 971–976. [CrossRef]

19. Biabani-Ravandi, A.; Rezaei, M. Low temperature CO oxidation over Fe-Co mixed oxide nanocatalysts. *Chem. Eng. J.* **2012**, *184*, 141–146. [CrossRef]

20. Shi, C.; Wang, Y.; Zhu, A.; Chen, B.; Au, C. $Mn_xCo_{3-x}O_4$ solid solution as high-efficient catalysts for low-temperature oxidation of formaldehyde. *Catal. Commun.* **2012**, *28*, 18–22. [CrossRef]

21. Zou, G.; Xu, Y.; Wang, S.; Chen, M.; Shangguan, W. The synergistic effect in Co-Ce oxides for catalytic oxidation of diesel soot. *Catal. Sci. Technol.* **2015**, *5*, 1084–1092. [CrossRef]

22. Li, D.; Wang, L.; Koike, M.; Nakagawa, Y.; Tomishige, K. Steam reforming of tar from pyrolysis of biomass over Ni/Mg/Al catalysts prepared from hydrotalcite-like precursors. *Appl. Catal. B Environ.* **2011**, *102*, 528–538. [CrossRef]

23. Zhang, X.; Zhao, M.; Song, Z.; Zhao, H.; Liu, W.; Zhao, J.; Ma, Z.; Xing, Y. The effect of different metal oxides on the catalytic activity of a Co_3O_4 catalyst for toluene combustion: Importance of the structure-property relationship and surface active species. *New J. Chem.* **2019**, *43*, 10868–10877. [CrossRef]

24. Zhang, Q.; Mo, S.; Chen, B.; Zhang, W.; Huang, C.; Ye, D. Hierarchical Co_3O_4 nanostructures in-situ grown on 3D nickel foam towards toluene oxidation. *Mol. Catal.* **2018**, *454*, 12–20. [CrossRef]

25. Biesinger, M.C.; Payne, B.P.; Grosvenor, A.P.; Lau, L.W.M.; Gerson, A.R.; Smart, R.S.C. Resolving surface chemical states in XPS analysis of first row transition metals, oxides and hydroxides: Cr, Mn, Fe, Co and Ni. *Appl. Surf. Sci.* **2011**, *257*, 2717–2730. [CrossRef]

26. Cañón, J.; Teplyakov, A.V. XPS characterization of cobalt impregnated SiO_2 and γ-Al_2O_3. *Surf. Interface Anal.* **2021**, *53*, 475–481. [CrossRef]

27. Cole, K.M.; Kirk, D.W.; Thorpe, S.J. Co_3O_4 nanoparticles characterized by XPS and UPS. *Surf. Sci. Spectra* **2021**, *28*, 014001. [CrossRef]

28. Ilieva, L.; Petrova, P.; Venezia, A.M.; Anghel, E.M.; State, R.; Avdeev, G.; Tabakova, T. Mechanochemically Prepared Co_3O_4-CeO_2 Catalysts for Complete Benzene Oxidation. *Catalysts* **2021**, *11*, 1316. [CrossRef]

29. Zasada, F.; Janas, J.; Piskorz, W.; Gorczynska, M.; Sojka, Z. Total oxidation of lean methane over cobalt spinel nanocubes controlled by the self-adjusted redox state of the catalyst: Experimental and theoretical account for interplay between the Langmuir-Hinshelwood and Mars-Van Krevelen mechanisms. *ACS Catal.* **2017**, *7*, 2853–2867. [CrossRef]

30. Rosen, J.; Hutchings, G.S.; Jiao, F. Ordered mesoporous cobalt oxide as highly efficient oxygen evolution catalyst. *J. Am. Chem. Soc.* **2013**, *135*, 4516–4521. [CrossRef] [PubMed]

31. Gu, C.; Li, Y.; Mo, Y.; Lan, J.; Jiang, Y.; Feng, S. Rod-like and mushroom-like Co_3O_4–CeO_2 catalysts derived from Ce-1,3,5-benzene tricarboxylic acid for CO preferential oxidation: Effects of compositions and morphology. *React. Kinet. Mech. Catal.* **2020**, *129*, 135–151. [CrossRef]

32. Zheng, Y.; Yu, Y.; Zhou, H.; Huang, W.; Pu, Z. Combustion of lean methane over Co_3O_4 catalysts prepared with different cobalt precursors. *RSC Adv.* **2020**, *10*, 4490–4498. [CrossRef]

33. Zasada, F.; Grybos, J.; Budiyanto, E.; Janas, J.; Sojka, Z. Oxygen species stabilized on the cobalt spinel nano-octahedra at various reaction conditions and their role in catalytic CO and CH_4 oxidation, N_2O decomposition and oxygen isotopic exchange. *J. Catal.* **2019**, *371*, 224–235. [CrossRef]

34. Xu, X.; Han, H.; Liu, J.; Liu, W.; Li, W.; Wang, X. Promotional effects of samarium on Co_3O_4 spinel for CO and CH_4 oxidation. *J. Rare Earth.* **2014**, *32*, 159–169. [CrossRef]

35. Li, G.; Li, N.; Sun, Y.; Qu, Y.; Jiang, Z.; Zhao, Z.; Zhang, Z.; Cheng, J.; Hao, Z. Efficient defect engineering in Co-Mn binary oxides for low-temperature propane oxidation. *Appl. Catal. B Environ.* **2021**, *282*, 119512. [CrossRef]

36. Choya, A.; de Rivas, B.; González-Velasco, J.R.; Gutiérrez-Ortiz, J.I.; López-Fonseca, R. Optimisation of bimetallic Co-Ni supported catalysts for oxidation of methane in natural gas vehicles. *Appl. Catal. B Environ.* **2021**, *284*, 119712. [CrossRef]

37. Rodrigues, J.M.; Ribeiro, M.F.; Fernandes, E.C. Catalytic activity of electrodeposited cobalt oxide films for methane combustion in a micro-channel reactor. *Fuel* **2018**, *232*, 51–59. [CrossRef]

38. Stefanov, P.; Todorova, S.; Naydenov, A.; Tzaneva, B.; Kolev, H.; Atanasova, G.; Stoyanova, D.; Karakirova, Y.; Aleksieva, K. On the development of active and stable Pd-Co/γ-Al$_2$O$_3$ catalyst for complete oxidation of methane. *Chem. Eng. J.* **2015**, *266*, 329–338. [CrossRef]

39. Nasr, S.; Hayes, R.E.; Semagina, N. Stability of kinetic parameters of Co$_3$O$_4$/CeO$_2$ catalyzed methane combustion. *Can. J. Chem. Eng.* **2021**, *99*, 2670–2676. [CrossRef]

40. Zasada, F.; Piskorz, W.; Janas, J.; Grybos, J.; Indyka, P.; Sojka, Z. Reactive oxygen species on the (100) facet of cobalt spinel nanocatalyst and their relevance in ^{16}O$_2$/^{18}O$_2$ isotopic exchange, *de*N$_2$O, and *de*CH$_4$ processes–A theoretical and experimental account. *ACS Catal.* **2015**, *5*, 6879–6892. [CrossRef]